



## Article

# Numerical Analysis on the Effect of the Conduction Band Offset in Dion–Jacobson Perovskite Solar Cells

Yongjin Gan <sup>1</sup>, Guixin Qiu <sup>2</sup>, Chenqing Yan <sup>1</sup>, Zhaoxiang Zeng <sup>1</sup>, Binyi Qin <sup>3,4</sup>, Xueguang Bi <sup>1,\*</sup>   
and Yucheng Liu <sup>5,\*</sup> 

<sup>1</sup> School of Physics and Telecommunication Engineering, Yulin Normal University, Yulin 537000, China; yongjin\_gan@ylyu.edu.cn (Y.G.); cqy@ylyu.edu.cn (C.Y.); zxz@ylyu.edu.cn (Z.Z.)

<sup>2</sup> Office of the Party Committee, Guangxi Minzu Normal University, Chongzuo 532200, China; gxq@ylyu.edu.cn

<sup>3</sup> Center for Applied Mathematics of Guangxi, Yulin Normal University, Yulin 537000, China; byqin@ylyu.edu.cn

<sup>4</sup> Guangxi Colleges and Universities Key Laboratory of Complex System Optimization and Big Data Processing, Yulin Normal University, Yulin 537000, China

<sup>5</sup> Department of Mechanical Engineering, South Dakota State University, Brookings, SD 57007, USA

\* Correspondence: xgb@ylyu.edu.cn (X.B.); yucheng.liu@sdstate.edu (Y.L.); Tel.: +86-138-0121-7945 (X.B.); +1-605-688-4287 (Y.L.)

**Abstract:** Benefiting from the advantages of a high absorption coefficient, a long charge diffusion length, excellent carrier mobility, and a tunable bandgap, three-dimensional (3D) metal halide perovskites exhibit great potential for application in solar cells. However, 3D perovskite solar cells (PSCs) often suffer from poor long-term stability against moisture, heat, and light. To address this issue, reducing the dimension of perovskite and forming two-dimensional (2D) perovskites can be effective in slowing down the oxidation of the perovskite film and significantly improving device stability. In this study, 2D PSCs were designed with glass/FTO/TiO<sub>2</sub>/Dion–Jacobson (DJ) perovskite/NiOx/Au structures, based on the solar cell simulation software SCAPS. The absorption layers employed in the study included PeDAMA<sub>2</sub>Pb<sub>3</sub>I<sub>10</sub>, PeDAMA<sub>3</sub>Pb<sub>4</sub>I<sub>13</sub>, PeDAMA<sub>4</sub>Pb<sub>5</sub>I<sub>16</sub>, and PeDAMA<sub>5</sub>Pb<sub>6</sub>I<sub>19</sub>. The influence of the conduction band offset (*CBO*) variation in the range of  $-0.5$  to  $0.5$  eV on cell performance was explored through a numerical simulation. The simulation results indicate that the open-circuit voltage and fill factor continue to increase, whereas the short-circuit current density remains almost unchanged when the *CBO* increases from  $-0.5$  eV to  $0$  eV. The devices exhibit better performance when the value of the *CBO* is positive and within a small range. For DJ PSCs, controlling the *CBO* within  $0.1$ – $0.4$  eV is conducive to better cell performance.

**Keywords:** solar cell; two-dimensional perovskites; SCAPS; conduction band offset; performance



**Citation:** Gan, Y.; Qiu, G.; Yan, C.; Zeng, Z.; Qin, B.; Bi, X.; Liu, Y. Numerical Analysis on the Effect of the Conduction Band Offset in Dion–Jacobson Perovskite Solar Cells. *Energies* **2023**, *16*, 7889. <https://doi.org/10.3390/en16237889>

Academic Editors: Philippe Leclère and Tapas Mallick

Received: 25 October 2023  
Revised: 18 November 2023  
Accepted: 30 November 2023  
Published: 2 December 2023



**Copyright:** © 2023 by the authors. Licensee MDPI, Basel, Switzerland. This article is an open access article distributed under the terms and conditions of the Creative Commons Attribution (CC BY) license (<https://creativecommons.org/licenses/by/4.0/>).

## 1. Introduction

As a research direction with great potential in the field of solar cells, the development of perovskite solar cells (PSCs) has experienced rapid growth. The power conversion efficiency (*PCE*) of PSCs has surged from only 3.8% in 2009 to an impressive 25.73% to 28.75% [1–4]. Three-dimensional (3D) metal halide perovskites demonstrate substantial promise for solar cell applications owing to their high absorption coefficient, long charge diffusion length, excellent carrier mobility, and tunable bandgap. However, the inherent drawback of 3D PSCs lies in their inferior long-term stability against moisture, heat, and light, limiting their commercial potential. Various strategies, including doping, component engineering, interfacial modification, the use of novel electron and hole transport materials, and encapsulation have been used to enhance the stability of PSCs. Recent studies suggest that reducing the dimension of perovskite and forming 2D perovskites by introducing hydrophobic organic cations [5–7] can effectively mitigate the oxidation of the perovskite film, significantly improving device stability. Dion–Jacobson (DJ) perovskite, characterized by a distinct stacked structure, is a common form of 2D perovskite. In DJ perovskites,

neighboring inorganic slabs are bridged by diammonium spacers without van der Waals gaps [8]. DJ perovskite PSCs exhibit superior optoelectronic characteristics and enhanced durability [9,10]. Despite these advantages, DJ PSCs face challenges related to serious non-radiative recombination in the bulk [11] and interface, resulting in poor carrier extraction and collection compared to 3D PSCs. Consequently, DJ PSCs still exhibit lower *PCEs* than their 3D counterparts.

To enhance the performance of DJ perovskite PSCs, numerous strategies have been proposed to optimize film quality, including compositional engineering [11], solvent engineering [12], additive addition [13], and an annealing process [14]. In 2019, Zheng et al. achieved *PCEs* of 14.16% and 16.38% by employing 1,3-propanediammonium (PDA) and 1,4-butanediammonium (BDA) to construct DJ PSCs, respectively. Their experimental results demonstrated that by controlling the thickness of the quantum well barrier, they could obtain DJ phase perovskites with better orientation and a more uniform distribution, thereby boosting the performance of DJ PSCs [15]. In 2021, Chen and colleagues fabricated DJ PSCs with a gradient energy band alignment in 2021 by coating FABr onto the perovskite films, resulting in an increase in the *PCE* from 13.78% to 16.75% [16]. Chen et al. also utilized a novel annealing process, combining pre-annealing and merged annealing, to modify the interface at the perovskite and charge-transporting layer, promoting charge transport [17]. To suppress surface defect density, Zhang et al. proposed a secondary anti-solvent strategy for DJ perovskite films which proved effective in preparing highly efficient DJ PSCs [18]. Mohammed et al. demonstrated through a numerical simulation that DJ PSCs with pentamethylenediamine spacers were promising for photovoltaic applications [19]. They optimized different parameters to improve solar cell performance and achieved a *PCE* of 21.17% [20]. In 2023, Zhai and coworkers proposed that charge recombination could be suppressed, interfacial charge accumulation restricted, and charge transport promoted by introducing an interlayer of polyaspartic acid at the interface of a hole-transporting layer (HTL) and a perovskite layer. With this optimization strategy, the *PCE* of a DJ PSC increased from 15.03% to 17.34% [21].

Many reported studies have confirmed that the characteristics of the interface between the perovskite layer and carrier transport layers have a direct impact on cell performance. The conduction band offset (*CBO*) between the perovskite layer and the electron transport layer (ETL) is an important feature of the interface. Therefore, there is a correlation between the *CBO* and cell performance. A suitable ETL should exhibit proper band alignment with the perovskite layer, ensuring that the transport of electrons is promoted while holes are hindered [22–24]. In order to achieve good band alignment between the perovskite layer and ETL, researchers have proposed many methods for interface engineering [25,26], such as doping the ETL with other elements to reach the optimal band alignment with the perovskite layer [22,23], adjusting the band structure via gradient doping [27], inserting a buffer layer between the perovskite layer and the ETL [28], or adjusting the electron affinity of the ETL to achieve proper band matching [29].

DJ PSCs were fabricated by incorporating bulky organic ammonium spacer pentamethylenediamine (PeDA) into DJ perovskite films with four different layer numbers: 3, 4, 5, and 6. These layer numbers correspond to PeDAMA<sub>2</sub>Pb<sub>3</sub>I<sub>10</sub>, PeDAMA<sub>3</sub>Pb<sub>4</sub>I<sub>13</sub>, PeDAMA<sub>4</sub>Pb<sub>5</sub>I<sub>16</sub>, and PeDAMA<sub>5</sub>Pb<sub>6</sub>I<sub>19</sub>, respectively. In this study, DJ PSCs, including PeDA-DAMA<sub>2</sub>Pb<sub>3</sub>I<sub>10</sub>-based PSCs, PeDAMA<sub>3</sub>Pb<sub>4</sub>I<sub>13</sub>-based PSCs, PeDAMA<sub>4</sub>Pb<sub>5</sub>I<sub>16</sub>-based PSCs, and PeDAMA<sub>5</sub>Pb<sub>6</sub>I<sub>19</sub>-based PSCs, were constructed and simulated using a one-dimensional (1D) solar cell simulation program, SCAPS. The focus of this simulation was on assessing the impact of the conduction band offset (*CBO*) between the DJ perovskite layer and the electron transport layer (ETL). To understand the operation mechanism of the devices, the relationship between the *CBO* in the range of  $-0.5$  eV to  $0.5$  eV and the performance of the DJ PSCs was analyzed. The evaluation indicators included the open-circuit voltage ( $V_{oc}$ ), short-circuit current density ( $J_{sc}$ ), fill factor (*FF*), *PCE*, recombination current, and recombination rate. The numerical simulation results presented in this article

offer significant guidance for the development and manufacturing of highly efficient DJ PSCs and provide a solid foundation for future advancements in solar energy technology.

## 2. Methods and Materials

### 2.1. Numerical Research Method

Studying PSCs through a numerical simulation can mitigate the influence of unrelated external factors and help researchers analyze the internal physical mechanisms of PSCs. This approach promotes the development of PSCs in experimental preparation. Therefore, in this study, a 1D numerical simulation software, SCAPS, developed by Professor Burgelman of Gent University in Belgium [30], was adopted as the research tool. SCAPS is widely used for numerical simulations of solar cells. Based on the fundamental equations of semiconductor device physics, including the Poisson equation, hole continuity equations, and electron continuity equations (Equations (1)–(3)) [31,32], SCAPS can calculate the current density–voltage characteristics ( $J$ - $V$ ), spectral response, capacitance–frequency characteristics ( $C$ - $F$ ), capacitance–voltage characteristics ( $C$ - $V$ ) band structures, carrier concentration, and spectral response under specific boundary conditions and has been extensively employed in numerical analyses of perovskite solar cells [3,4,33]. Specific operating parameters such as bias voltage, frequency, and temperature are set in SCAPS before running the simulation model.

$$-\frac{\partial}{\partial x} \left( \varepsilon(x) \frac{\partial V}{\partial x} \right) = q [p(x)n(x) + N_D^+(x) - N_A^-(x) + p_t(x) - n_t(x)] \quad (1)$$

$$\frac{\partial p}{\partial t} = \frac{1}{q} \frac{\partial J_p}{\partial x} + G_p - R_p \quad (2)$$

$$\frac{\partial n}{\partial t} = \frac{1}{q} \frac{\partial J_n}{\partial x} + G_n - R_n \quad (3)$$

In the equations above,  $q$  represents the electronic charge,  $\varepsilon$  is the dielectric constant,  $V$  stands for the potential, and  $p(x)$  and  $n(x)$  denote the concentrations of free holes and electrons, respectively. Additionally,  $N_D^+$  and  $N_A^-$  are the donor and acceptor densities, while  $p_t(x)$  and  $n_t(x)$  represent the concentrations of hole traps and electron traps, respectively.  $J_n$  and  $J_p$  correspond to the current density of electrons and the current density of holes, respectively, and  $G_n$  and  $G_p$  signify the generation rates of electrons and holes.  $R_n$  and  $R_p$  represent the recombination rates of electrons and holes, respectively. A previous study also presented advanced experimental tools for characterizing PSC performance [34].

### 2.2. Model Structure and Material Parameters

Using SCAPS, we designed an N-I-P PSC with the structure glass/FTO/ETL/DJ perovskite/HTL/Au, as shown in Figure 1a. In this figure,  $\text{TiO}_2$  and  $\text{NiO}_x$  were employed as the ETL and HTL, respectively. FTO served as the front contact, while Au acted as the metal back electrode. The DJ perovskite, encompassing  $\text{PeDAMA}_2\text{Pb}_3\text{I}_{10}$ ,  $\text{PeDAMA}_3\text{Pb}_4\text{I}_{13}$ ,  $\text{PeDAMA}_4\text{Pb}_5\text{I}_{16}$ , and  $\text{PeDAMA}_5\text{Pb}_6\text{I}_{19}$ , functioned as the active layer. Figure 1b depicts the energy levels of different materials. Excitons are generated when perovskite materials absorb photons with energies exceeding their bandgaps. Subsequently, the excitons migrate to the interface between the perovskite layers and the carrier transport layers, forming free electrons and free holes. These free electrons and free holes then traverse the ETL and HTL, respectively, and are ultimately collected by the corresponding electrodes.

The material parameter settings for constructing the initial models [14,18,25,26] and the interface parameters of the  $\text{NiO}_x$ /DJ perovskite and DJ perovskite/ $\text{TiO}_2$  [19,27] were derived from authoritative studies to ensure the reliability of the simulation reference data sources. In Figure 2,  $J$ - $V$  characteristic curves are presented for devices under the conditions of dark and light. Figure 2a–d correspond to  $\text{PeDAMA}_2\text{Pb}_3\text{I}_{10}$ ,  $\text{PeDAMA}_3\text{Pb}_4\text{I}_{13}$ ,  $\text{PeDAMA}_4\text{Pb}_5\text{I}_{16}$ , and  $\text{PeDAMA}_5\text{Pb}_6\text{I}_{19}$ , respectively. The diode rectification character-

istics in all four initial models indicate the reliability of the structural design. Figure 3a demonstrates an improvement in the *J-V* characteristic curve when transitioning from  $\text{PeDAMA}_2\text{Pb}_3\text{I}_{10}$  to  $\text{PeDAMA}_5\text{Pb}_6\text{I}_{19}$ . Figure 3b explains this phenomenon. Among the four types of perovskite materials, the bandgap order from large to small is  $\text{PeDAMA}_2\text{Pb}_3\text{I}_{10} > \text{PeDAMA}_3\text{Pb}_4\text{I}_{13} > \text{PeDAMA}_4\text{Pb}_5\text{I}_{16} > \text{PeDAMA}_5\text{Pb}_6\text{I}_{19}$ . Consequently, the absorption of photons gradually improves from  $\text{PeDAMA}_2\text{Pb}_3\text{I}_{10}$  to  $\text{PeDAMA}_5\text{Pb}_6\text{I}_{19}$ , indicating that  $\text{PeDAMA}_5\text{Pb}_6\text{I}_{19}$  and  $\text{PeDAMA}_2\text{Pb}_3\text{I}_{10}$  have the best and worst absorption of photons, respectively. Hence,  $\text{PeDAMA}_5\text{Pb}_6\text{I}_{19}$ -based solar cells have the optimal quantum efficiency (*QE*), while  $\text{PeDAMA}_2\text{Pb}_3\text{I}_{10}$ -based solar cells have the lowest *QE*. In general, all initial models exhibit good photon absorption below 780 nm, confirming their reliability. Therefore, the following section will explore the impact of the interface band offset between the ETL ( $\text{TiO}_2$ ) and the perovskite layer on the cell performance based on these models. Table 1 listed the basic parameters of the initial model while Table 2 displays key interface parameter settings.

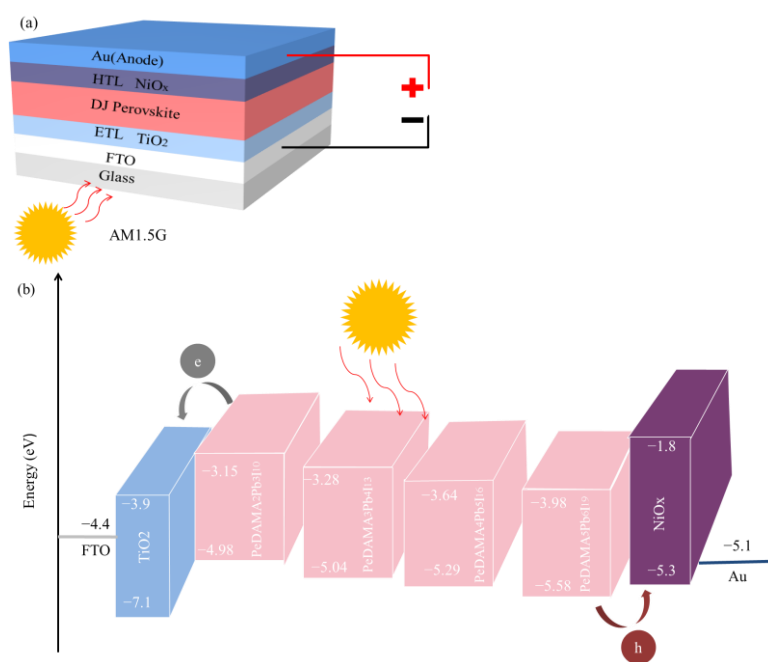


**Figure 1.** Initial model and its energy band structure: (a) initial model structure; (b) energy band structure diagram.

**Table 1.** Basic parameters of the initial model.

Parameter	NiO <sub>x</sub>	PeDAMA <sub>2</sub> Pb <sub>3</sub> I <sub>10</sub>	PeDAMA <sub>3</sub> Pb <sub>4</sub> I <sub>13</sub>	PeDAMA <sub>4</sub> Pb <sub>5</sub> I <sub>16</sub>	PeDAMA <sub>5</sub> Pb <sub>6</sub> I <sub>19</sub>	TiO <sub>2</sub>
Thickness/nm	100	800	800	800	800	50
Band gap/eV	3.5	1.83	1.76	1.65	1.6	3.2
Electron affinity/eV	1.8	3.15	3.28	3.64	3.98	3.9
Dielectric permittivity	10.7	25	25	25	25	9
Electron mobility/cm <sup>2</sup> /V.s	12	1.4	1.4	1.4	1.4	20
Hole mobility/cm <sup>2</sup> /V.s	2.8	0.3	0.3	0.3	0.3	10
Acceptor concentration/cm <sup>-3</sup>	$3.0 \times 10^{18}$	0	0	0	0	0
Donor concentration/cm <sup>-3</sup>	0	0	0	0	0	$1.0 \times 10^{-16}$
CB effective density of states/cm <sup>-3</sup>	$2.8 \times 10^{19}$	$7.5 \times 10^{17}$	$7.5 \times 10^{17}$	$7.5 \times 10^{17}$	$7.5 \times 10^{17}$	$1.0 \times 10^{21}$
VB effective density of states/cm <sup>-3</sup>	$1.0 \times 10^{18}$	$1.8 \times 10^{18}$	$1.8 \times 10^{18}$	$1.8 \times 10^{18}$	$1.8 \times 10^{18}$	$2.0 \times 10^{20}$
Defect type	Neutral	Neutral	Neutral	Neutral	Neutral	Neutral
Capture cross-section for electrons/cm <sup>2</sup>	$1.0 \times 10^{-15}$	$1.0 \times 10^{-15}$	$1.0 \times 10^{-15}$	$1.0 \times 10^{-15}$	$1.0 \times 10^{-15}$	$1.0 \times 10^{-15}$
Capture cross-section for holes/cm <sup>2</sup>	$1.0 \times 10^{-15}$	$1.0 \times 10^{-15}$	$1.0 \times 10^{-15}$	$1.0 \times 10^{-15}$	$1.0 \times 10^{-15}$	$1.0 \times 10^{-15}$
Total defect density/cm <sup>-3</sup>	$1.0 \times 10^{-15}$	$2.5 \times 10^{-14}$	$2.5 \times 10^{-14}$	$2.5 \times 10^{-14}$	$2.5 \times 10^{-14}$	$1.0 \times 10^{-16}$

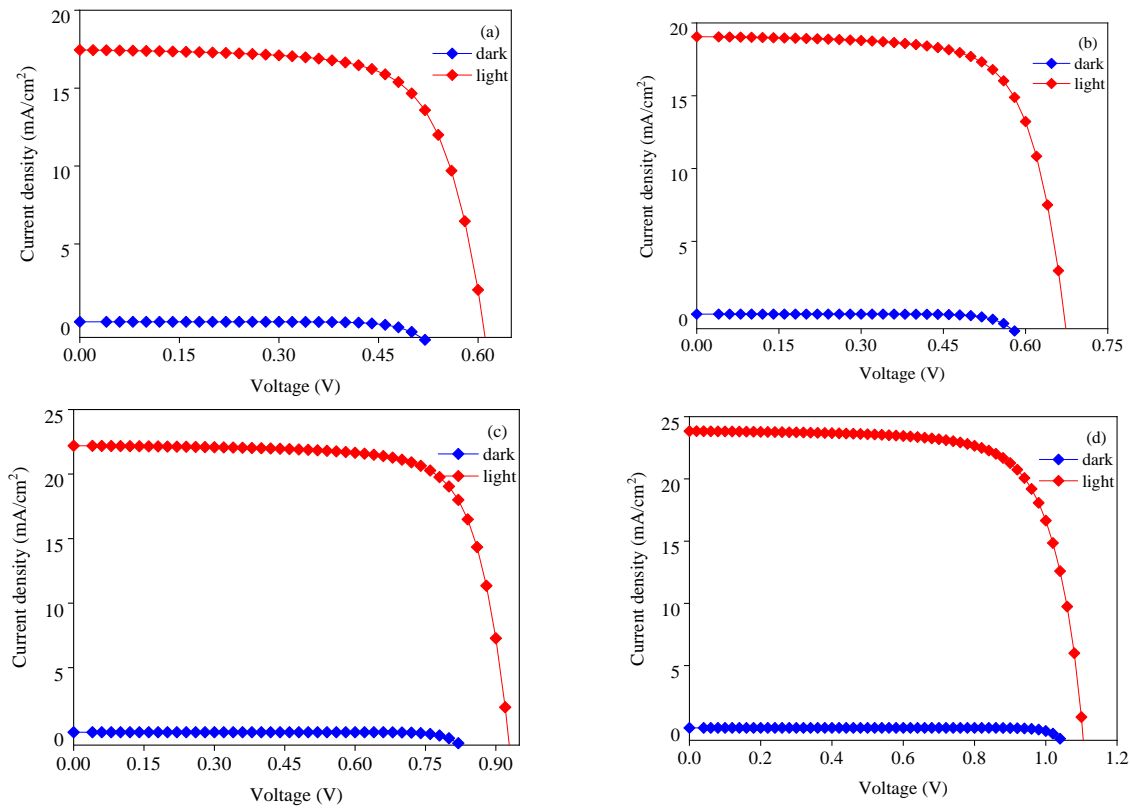


**Figure 2.** *J-V* characteristic curves of the initial models under different illumination conditions: (a) PeDAMA<sub>2</sub>Pb<sub>3</sub>I<sub>10</sub>-based model; (b) PeDAMA<sub>3</sub>Pb<sub>4</sub>I<sub>13</sub>-based model; (c) PeDAMA<sub>4</sub>Pb<sub>5</sub>I<sub>16</sub>-based model; (d) PeDAMA<sub>5</sub>Pb<sub>6</sub>I<sub>19</sub>-based model.

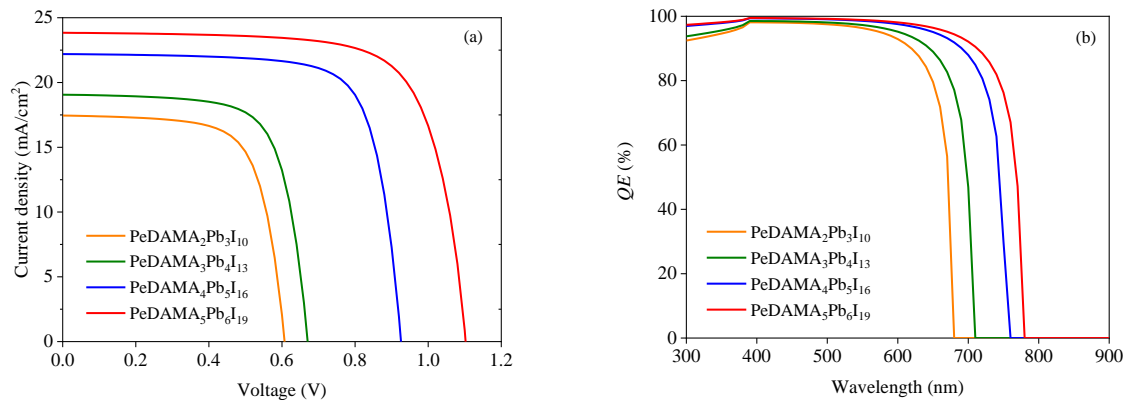


**Figure 3.** *J-V* characteristic curves and quantum efficiency curves of the initial models: (a) *J-V* characteristic curves; (b) quantum efficiency curves.

**Table 2.** Interface parameter settings.

Parameter	NiOx/DJ Perovskite	DJ Perovskite/TiO <sub>2</sub>
Type of Defect	Neutral	Neutral
Cross-Section for Electron Capture/cm <sup>2</sup>	$1.0 \times 10^{-15}$	$1.0 \times 10^{-15}$
Cross-Section for Hole Capture/cm <sup>2</sup>	$1.0 \times 10^{-15}$	$1.0 \times 10^{-15}$
Distribution of Energies	single	single
Reference for Energy Level of Defect	Above the highest $E_v$	Above the highest $E_v$
Energy with Respect to Reference/eV	0.6	0.6
Total Density of Defects/cm <sup>-3</sup>	$1.0 \times 10^{10}$	$1.0 \times 10^{10}$

### 3. Results and Discussion

Figure 4 illustrates a schematic of the barrier structure at the interface between the perovskite layer and the ETL. The *CBO*, which stands for conduction band offset, quantifies the misalignment between the conduction band of the perovskite and the ETL. The *CBO* value is calculated by subtracting the conduction band level of the perovskite from that of the ETL. The magnitude of the *CBO* is closely related to the interface barrier. The *CBO* is negative when the conduction band level of the ETL is lower than that of the perovskite, and it is positive when the conduction band level of the ETL is higher. As depicted in Figure 4a, a negative *CBO* results in an energy cliff at the interface between the perovskite layer and the ETL. Conversely, in Figure 4b, a positive *CBO* leads to the formation of an energy spike at the same interface. The structural difference between a cliff and a spike is significant. An energy cliff does not impede the movement of photo-generated electrons, while an energy spike acts as an obstacle. Consequently, the energy required for a photo-generated electron to traverse these different barriers varies, leading to variations in the accumulation and interface recombination of carriers.

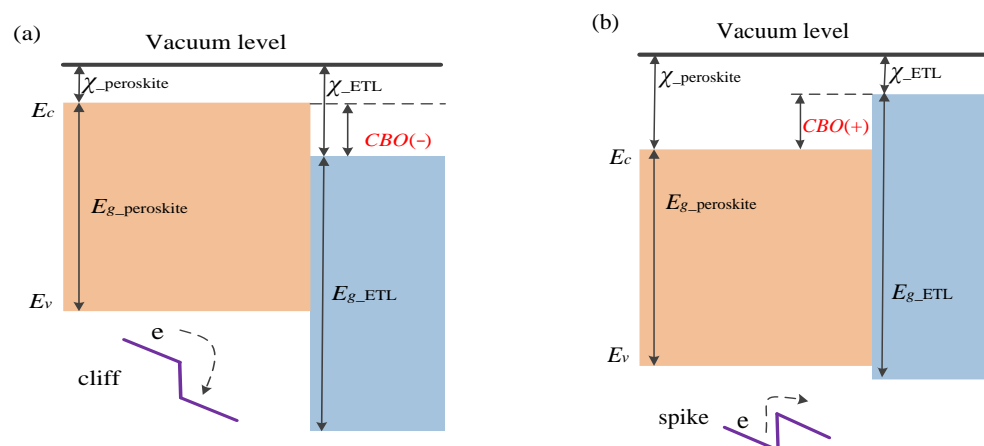


**Figure 4.** Schematic of the barrier structure at the interface between perovskite and ETL: (a) *CBO* is negative; (b) *CBO* is positive.

The *CBO* has a significant impact on interface recombination which is both theoretically supported [35–37] and experimentally demonstrated [38–40]. To analyze the relationship between the *CBO* and the performance of the DJ PSCs in this study, we maintained the *CBO* within the range of  $-0.5$  to  $0.5$  eV. The simulation work adopted the control variable method. To control the value of the *CBO*, the electron affinity of the ETL was altered, while the other parameters of the materials listed in Table 1 remained unchanged. Figures 5 and 6 display the simulation results. Figure 5 illustrates the trends in the cell output parameters ( $V_{oc}$ ,  $J_{sc}$ ,  $FF$ , and  $PCE$ ) with different *CBO* values, while the corresponding  $J$ - $V$  characteristic curves are presented in Figure 6.

In Figure 5, when *CBO* values are negative, the  $V_{oc}$ ,  $FF$ , and  $PCE$  consistently increase from  $-0.5$  eV to  $0$  eV, while the  $J_{sc}$  remains relatively unchanged. Conversely, positive *CBO* values in the range of  $0.1$ – $0.4$  eV show less significant differences in output parameters which are larger than those observed in the negative range. However, with a further increase in the *CBO*, the cell performance rapidly declines. Similar trends are observed in Figure 6, in which  $J$ - $V$  characteristic curves steadily increase as the *CBO* changes from  $-0.5$  eV to  $0$  eV, almost overlapping and improving from  $0.1$ – $0.4$  eV but exhibiting a severe S-shape when the *CBO* reaches  $0.5$  eV.

When the *CBO* is less than  $0$  eV, a cliff forms at the interface between the ETL and the perovskite. Conversely, when the *CBO* is positive, a spike forms, as depicted in Figures 7 and 8, demonstrating a high degree of consistency between simulation results and theory. The activation energy for carrier recombination ( $E_a$ ) assesses carrier recombination at the interface between the perovskite and the ETL. For positive *CBO* values, the  $E_a$  equals



the band gap of the perovskite. In contrast, for a negative  $CBO$ , the  $E_a$  is defined by the difference between the band gap of the perovskite and the absolute value of the  $CBO$ . Consequently, negative  $CBO$  values increase the likelihood of interface recombination.

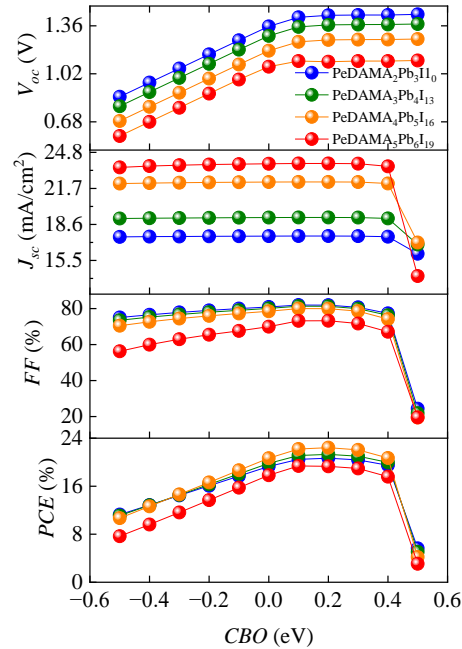


**Figure 5.** Trends in the cell output parameters with a change in the  $CBO$ .

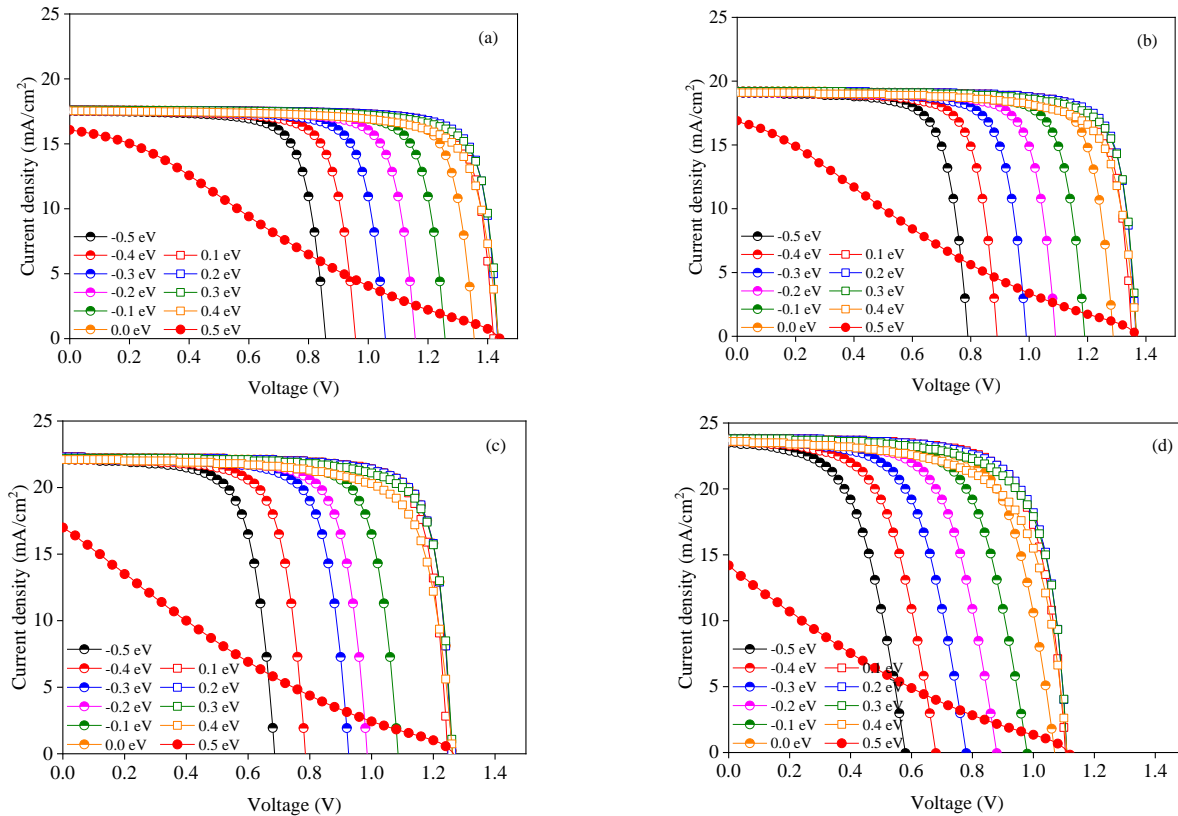


**Figure 6.**  $J$ - $V$  characteristic curves under different  $CBO$ s for different models: (a) PeDAMA<sub>2</sub>Pb<sub>3</sub>I<sub>10</sub>-based model; (b) PeDAMA<sub>3</sub>Pb<sub>4</sub>I<sub>13</sub>-based model; (c) PeDAMA<sub>4</sub>Pb<sub>5</sub>I<sub>16</sub>-based model; (d) PeDAMA<sub>5</sub>Pb<sub>6</sub>I<sub>19</sub>-based model.

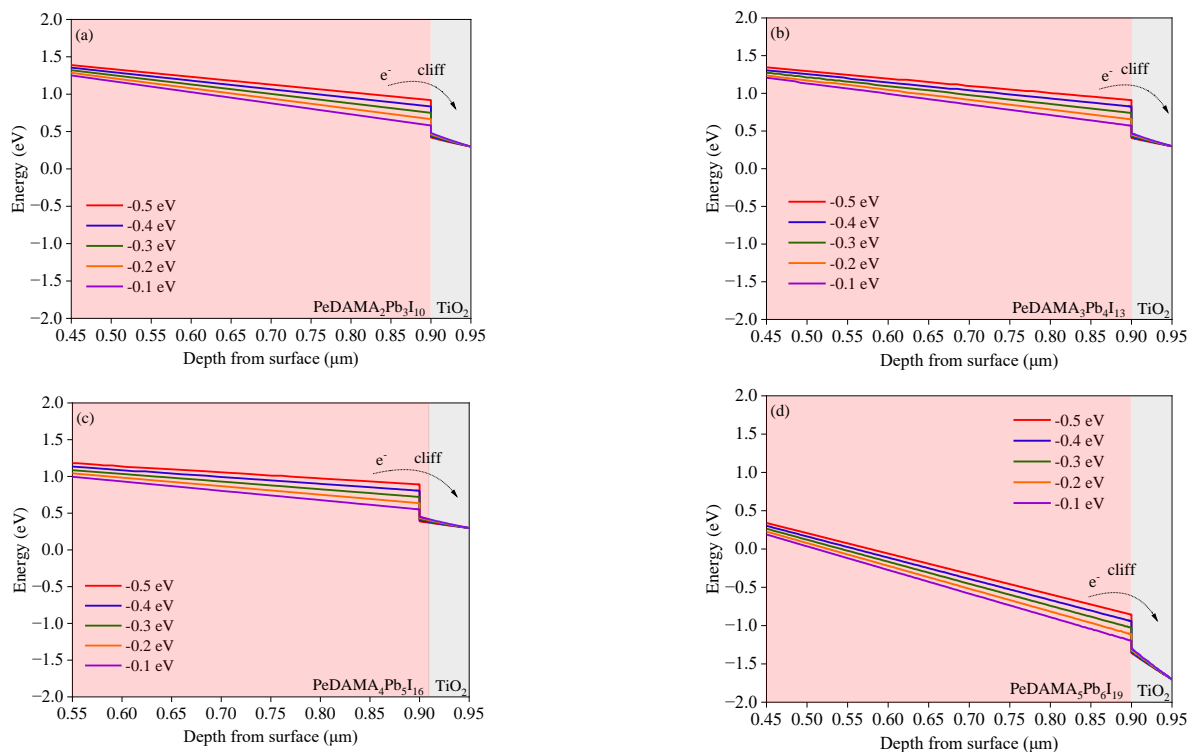


**Figure 7.** Interface band structures of DJ PSCs with negative CBOs: (a) PeDAMA<sub>2</sub>Pb<sub>3</sub>I<sub>10</sub>, (b) PeDAMA<sub>3</sub>Pb<sub>4</sub>I<sub>13</sub>, (c) PeDAMA<sub>4</sub>Pb<sub>5</sub>I<sub>16</sub>, and (d) PeDAMA<sub>5</sub>Pb<sub>6</sub>I<sub>19</sub>.

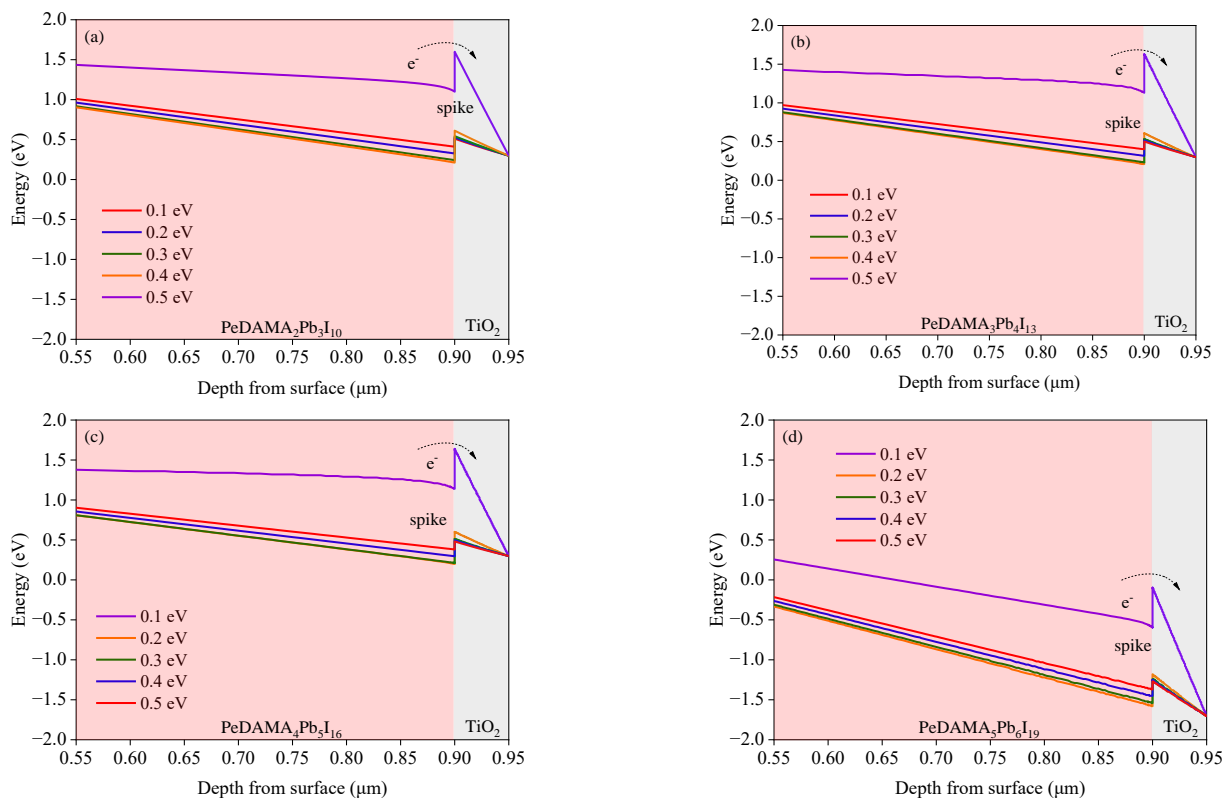


**Figure 8.** Interface band structures of DJ PSCs with positive CBOs: (a) PeDAMA<sub>2</sub>Pb<sub>3</sub>I<sub>10</sub>, (b) PeDAMA<sub>3</sub>Pb<sub>4</sub>I<sub>13</sub>, (c) PeDAMA<sub>4</sub>Pb<sub>5</sub>I<sub>16</sub>, and (d) PeDAMA<sub>5</sub>Pb<sub>6</sub>I<sub>19</sub>.



The formation of an energy cliff occurs as the  $CBO$  increases from  $-0.5$  eV to  $0$  eV. This energy cliff, while not impeding the movement of photo-generated electrons, results in a nearly unchanged  $J_{sc}$ . However, the activation energy  $E_a$  is smaller than the band gap of the perovskite, indicating that interface recombination predominantly influences the recombination mechanism [41–43]. Research has generally proven that  $V_{oc}$  is closely tied to carrier recombination. Low carrier recombination has a positive effect on promoting  $V_{oc}$ . The  $E_a$  measures the difficulty of carrier recombination. Carriers are more likely to recombine when the  $E_a$  is smaller. Therefore, it can be inferred that the  $E_a$  directly influences  $V_{oc}$ . As the  $CBO$  gradually increases from  $-0.5$  eV to  $0$  eV, the  $E_a$  also increases, leading to a gradual reduction in the likelihood of carrier recombination. Consequently, the  $V_{oc}$  shows a continuous increase. Both Figures 9 and 10 confirm that interface carrier recombination decreases gradually with an increase in the  $CBO$  from  $-0.5$  eV to  $0$  eV. The decrease in carrier recombination signifies a reduction in the internal consumption of the device, contributing to a gradual increase in the  $FF$ . The concurrent increases in the  $V_{oc}$  and  $FF$  further promote an overall rise in the  $PCE$ .

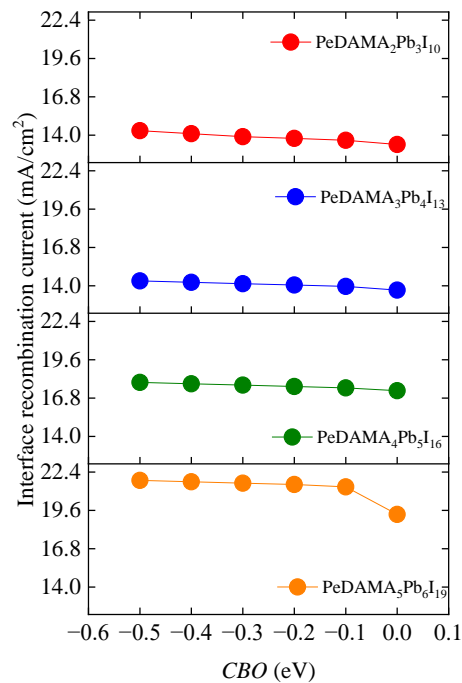


**Figure 9.** Interface recombination current at the perovskite/ETL interface when the  $CBO$  is negative.

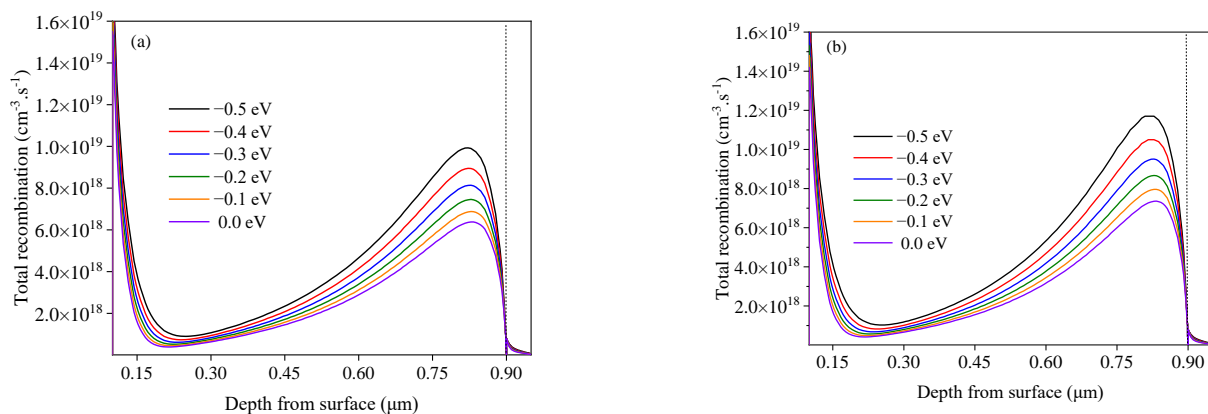


**Figure 10.** Cont.

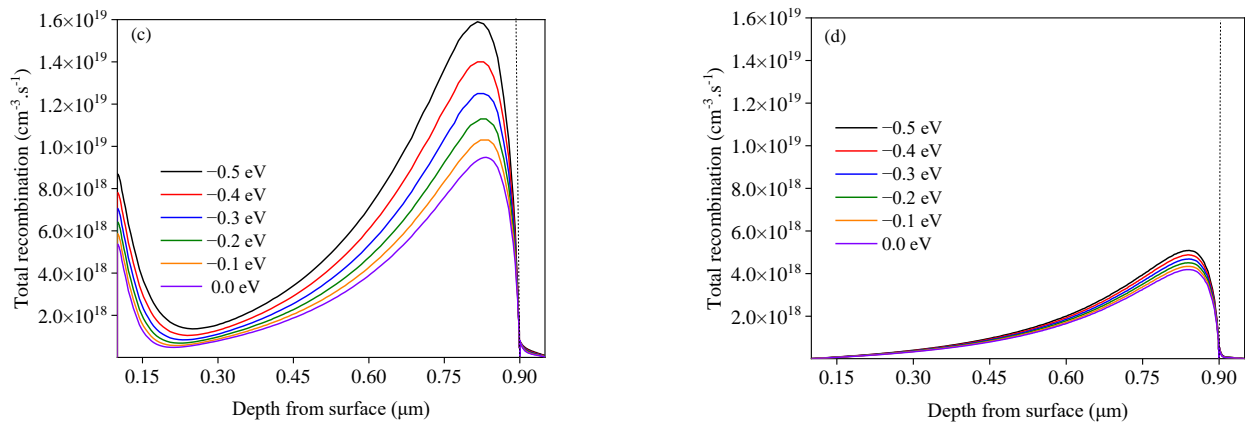


**Figure 10.** Total recombination at the perovskite/ETL interface when the *CBO* is negative. (a) PeDAMA<sub>2</sub>Pb<sub>3</sub>I<sub>10</sub>, (b) PeDAMA<sub>3</sub>Pb<sub>4</sub>I<sub>13</sub>, (c) PeDAMA<sub>4</sub>Pb<sub>5</sub>I<sub>16</sub>, and (d) PeDAMA<sub>5</sub>Pb<sub>6</sub>I<sub>19</sub>.

When the *CBO* ranges from 0.1 eV to 0.4 eV, an energy spike is formed. At this point, the  $E_a$  remains constant and is equal to the band gap of the perovskite, resulting in minimal differences in interface carrier recombination. Figure 11 illustrates that when the *CBO* is within this range, the fluctuation of the interface recombination current is weak, indicating insignificant changes in interface carrier recombination. Consequently, the  $V_{oc}$  and  $FF$  almost remain unchanged. It has been demonstrated that a spike within this small range has a limited effect on the motion of photo-generated electrons [31]. As a result,  $J_{sc}$  experiences little change. The negligible variations in the  $V_{oc}$ ,  $J_{sc}$ , and  $FF$  translate to insignificant changes in the  $PCE$ . However, if the *CBO* further increases to 0.5 eV, it may induce a double-diode-like curvature, leading to a rapid decrease in the  $FF$ . Consequently, the  $PCE$  experiences a significant decrease.

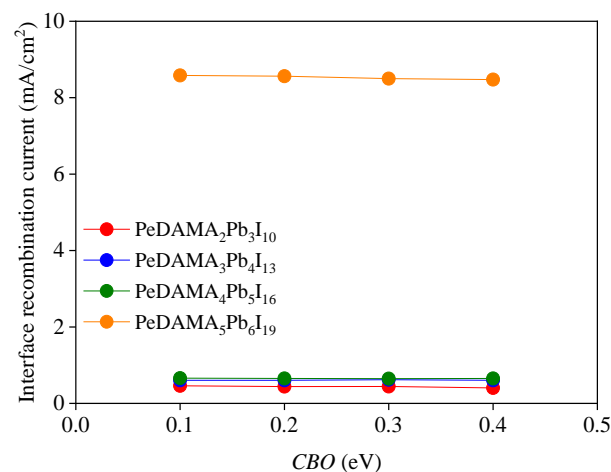


**Figure 11.** Interface recombination current at the perovskite/ETL interface with a positive *CBO*.

The cells perform better when the *CBO* is in the range of 0.1–0.4 eV than when the *CBO* is negative. A positive *CBO* leads to the formation of an energy spike, which acts as a barrier and impedes the transport and collection of photo-generated electrons. However, research has shown that a spike within a small range has less effect on the motion of photo-generated electrons but a greater impact on the carrier recombination rate [31]. In other words, PSCs may achieve better performance when an energy spike forms at the interface between the perovskite and the ETL. Therefore, the  $E_a$  has a stronger impact when a spike is formed, and the cell performance improves when the *CBO* is positive and there is a spike within a small range. Figures 5 and 6 demonstrate that controlling the *CBO* within 0.1–0.4 eV is beneficial for the better performance of DJ PSCs.

#### 4. Conclusions

The effects of the CBOs of DJ PSCs were analyzed using the 1D solar cell simulator SCAPS. The CBO is negative when the ETL has a lower conduction band level than the DJ perovskite and vice versa. An energy cliff is formed at the interface between the DJ perovskite and ETL when the CBO is negative, and an energy spike is generated when the CBO is positive. When the CBO is negative and a cliff is formed, the movement of electrons is not suppressed, so  $J_{sc}$  remains almost unchanged. However, the  $E_a$  gradually increases with an increase in the CBO, reducing the interface carrier recombination, leading to continuous increases with increases in the  $V_{oc}$  and  $FF$ . Thus, the  $PCE$  is improved. When the CBO is positive and a spike is generated, the  $E_a$  is equal to the band gap of the DJ perovskite, so the  $V_{oc}$  and  $FF$  remain almost unchanged. It has been proven that the  $E_a$  has a more significant impact on cell performance when the CBO is relatively small, and simulation results indicate that when the CBO is 0.1–0.4 eV, the performances of DJ PSCs improve. These numerical simulation results should provide important guidelines for designing efficient DJ PSCs.

**Author Contributions:** Conceptualization, Y.G. and B.Q.; methodology, Y.G. and Z.Z.; software, C.Y. and G.Q.; validation, Y.G. and B.Q.; formal analysis, X.B.; investigation, Y.G. and C.Y.; data curation, X.B.; writing—original draft preparation, Y.G.; writing—review and editing, Y.L.; visualization, C.Y.; supervision, X.B. and Y.L. All authors have read and agreed to the published version of the manuscript.

**Funding:** This research was funded by the high-quality talents research startup fund from Yulin Normal University (G2019ZK24), a Guangxi Key Laboratory of optoelectronic information processing project (GD21101), a Guangxi University Young and Middle-aged Teachers' Basic Scientific Research Ability Improvement Project (2022KY0580) and the Innovation and Entrepreneurship Training Program for College Students (202310606024, 202310606231).

**Data Availability Statement:** The data that support the findings of this study are available from the corresponding author upon reasonable request.

**Acknowledgments:** The authors are grateful to Marc Bergelman from the University of Gent for providing the SCAPS simulation program.

**Conflicts of Interest:** The authors declare no conflict of interest.

#### References

1. Kojima, A.; Teshima, K.; Shirai, Y.; Miyasaka, T. Organometal Halide Perovskites as Visible-Light Sensitizers for Photovoltaic Cells. *J. Am. Chem. Soc.* **2009**, *131*, 6050–6051. [\[CrossRef\]](#)
2. Park, J.; Kim, J.; Yun, H.S.; Paik, M.J.; Noh, E.; Mun, H.J.; Kim, M.G.; Shin, T.J.; Seok, S.I. Controlled Growth of Perovskite Layers with Volatile Alkylammonium Chlorides. *Nature* **2023**, *616*, 724–730. [\[CrossRef\]](#) [\[PubMed\]](#)
3. Gan, Y.-J.; Bi, X.-G.; Liu, Y.-C.; Qin, B.-Y.; Li, Q.-L.; Jiang, Q.-B.; Mo, P. Numerical Investigation Energy Conversion Performance of Tin-Based Perovskite Solar Cells using Cell Capacitance Simulator. *Energies* **2020**, *13*, 5907. [\[CrossRef\]](#)
4. Gan, Y.-J.; Zhao, D.; Qin, B.-Y.; Bi, X.-G.; Liu, Y.-C.; Ning, W.-L.; Yang, R.-Z.; Jiang, Q.-B. Numerical Simulation of High-Performance CsPbI<sub>3</sub>/FAPbI<sub>3</sub> Heterojunction Perovskite Solar Cells. *Energies* **2022**, *15*, 7301. [\[CrossRef\]](#)
5. Shao, M.; Bie, T.; Yang, L.; Gao, Y.; Jin, X.; He, F.; Zheng, N.; Yu, Y.; Zhang, X. Over 21% Efficiency Stable 2D Perovskite Solar Cells. *Adv. Mater.* **2022**, *34*, 2107211. [\[CrossRef\]](#) [\[PubMed\]](#)
6. Chen, J.; Wang, B.; Huang, G.; Cheng, Q.; Li, Y.; Li, X.; Li, S.; Li, K.; Zhu, L.; Zhai, Z.; et al. Thermally Regulated Energy Loss in Dion-Jacobson Perovskite Solar Cells. *Sol. RRL* **2022**, *6*, 2200636. [\[CrossRef\]](#)
7. Huang, G.; Chen, J.; Wang, B.; Cheng, Q.; Li, Y.; Zafar, S.U.; Yue, T.; Yan, Y.; Du, W.; Zhang, H.; et al. Solvent Effect on Film Formation and Trap States of Two Dimensional Dion-Jacobson Perovskite. *Nano Lett.* **2022**, *22*, 7545–7553. [\[CrossRef\]](#)
8. Mao, L.; Ke, W.; Pedesseau, L.; Wu, Y.; Katan, C.; Even, J.; Wasielewski, M.R.; Stoumpos, C.C.; Kanatzidis, M.G. Hybrid Dion-Jacobson 2D Lead Iodide Perovskites. *J. Am. Chem. Soc.* **2018**, *140*, 3775–3783. [\[CrossRef\]](#)
9. Stoumpos, C.C.; Cao, D.H.; Clark, D.J.; Young, J.; Rondinelli, J.M.; Jang, J.I.; Hupp, J.T.; Kanatzidis, M.G. Ruddlesden–Popper hybrid lead iodide perovskite 2D homologous semiconductors. *Chem. Mater.* **2016**, *28*, 2852–2867. [\[CrossRef\]](#)
10. Dong, Y.; Dong, X.; Lu, D.; Chen, M.; Zheng, N.; Wang, R.; Li, Q.; Xie, Z.; Liu, Y. Orbital interactions between the organic semiconductor spacer and the inorganic layer in dion-jacobson perovskites enable efficient solar cells. *Adv. Mater.* **2023**, *35*, 2205258. [\[CrossRef\]](#)

11. Mohammed, M.K.; Al-Mousoi, A.K.; Kumar, A.; Sabugaa, M.M.; Seemaladinne, R.; Pandey, R.; Al-Kahtani, A.A. Harnessing the potential of Dion-Jacobson perovskite solar cells: Insights from SCAPS simulation techniques. *J. Alloys Compd.* **2023**, *963*, 171246. [[CrossRef](#)]
12. Xiang, J.; Li, X.; Gong, S.; Wang, S.; Chen, X.; Zhang, F. Green Antisolvent-Induced Homogeneous Phase Distribution for Efficient and Stable MA-Free 2D Perovskite Solar Cells. *Chem. Eng. J.* **2023**, *460*, 141758. [[CrossRef](#)]
13. Chen, Y.; Hu, J.; Xu, Z.; Jiang, Z.; Chen, S.; Xu, B.; Xiao, X.; Liu, X.; Forberich, K.; Brabec, C.J.; et al. Managing Phase Orientation and Crystallinity of Printed Dion-Jacobson 2D Perovskite Layers via Controlling Crystallization Kinetics. *Adv. Funct. Mater.* **2022**, *32*, 2112146. [[CrossRef](#)]
14. Wu, H.; Lian, X.; Tian, S.; Zhang, Y.; Qin, M.; Zhang, Y.; Wang, F.; Lu, X.; Wu, G.; Chen, H. Additive-Assisted Hot-Casting Free Fabrication of Dion-Jacobson 2D Perovskite Solar Cell with Efficiency Beyond 16%. *Sol. RRL* **2020**, *4*, 2070074. [[CrossRef](#)]
15. Zhang, X.; Yang, T.; Ren, X.; Zhang, L.; Zhao, K.; Liu, S. Film Formation Control for High Performance Dion-Jacobson 2D Perovskite Solar Cells. *Adv. Energy Mater.* **2021**, *11*, 2002733. [[CrossRef](#)]
16. Zheng, Y.; Niu, T.; Qiu, J.; Chao, L.; Li, B.; Yang, Y.; Li, Q.; Lin, C.; Gao, X.; Zhang, C. Oriented and uniform distribution of Dion-Jacobson phase perovskites controlled by quantum well barrier thickness. *Sol. Rrl* **2019**, *3*, 1900090. [[CrossRef](#)]
17. Su, P.; Bai, L.; Bi, H.; Liu, B.; Chen, S.; Lee, D.; Yang, H.; Chen, C.; Zang, Z.; Chen, J. Interfacial Gradient Energy Band Alignment Modulation via Ion Exchange Reaction toward Efficient and Stable Methylammonium-Free Dion-Jacobson Quasi-2D Perovskite Solar Cells. *J. Power Sources* **2021**, *506*, 230213. [[CrossRef](#)]
18. Wu, H.; Lian, X.; Li, J.; Zhang, Y.; Zhou, G.; Wen, X.; Xie, Z.; Zhu, H.; Wu, G.; Chen, H. Merged Interface Construction toward Ultra-Low  $V_{oc}$  Loss in Inverted Two-Dimensional Dion-Jacobson Perovskite Solar Cells with Efficiency over 18. *J. Mater. Chem. A* **2021**, *9*, 12566–12573. [[CrossRef](#)]
19. Jin, L.; Ren, N.; Wang, P.; Li, R.; Xue, Q.; Huang, F.; Zhang, X.; Zhao, Y.; Zhang, X. Secondary Anti-Solvent Treatment for Efficient 2D Dion-Jacobson Perovskite Solar Cells. *Small* **2023**, *19*, 2205088. [[CrossRef](#)]
20. Zhai, Z.; Chen, J.; Liu, Q.; Jiang, S.; Li, Y. Defect Regulation of Efficient Dion-Jacobson Quasi-2D Perovskite Solar Cells via a Polyaspartic Acid Interlayer. *ACS Appl. Mater. Interfaces* **2023**, *15*, 38068–38079. [[CrossRef](#)]
21. Burgelman, M.; Nollet, P.; Degraeve, S. Modelling polycrystalline semiconductor solar cells. *Thin Solid films* **2000**, *361*, 527–532. [[CrossRef](#)]
22. Lee, K.M.; Lin, W.J.; Chen, S.H.; Wu, M.C. Control of TiO<sub>2</sub> electron transport layer properties to enhance perovskite photovoltaics performance and stability. *Org. Electron.* **2020**, *77*, 105406. [[CrossRef](#)]
23. Wu, M.C.; Chan, S.H.; Lee, K.M.; Chen, S.H.; Jao, M.H.; Chen, Y.F.; Su, W.F. Enhancing the efficiency of perovskite solar cells using mesoscopic zinc-doped TiO<sub>2</sub> as the electron extraction layer through band alignment. *J. Mater. Chem. A* **2018**, *6*, 16920–16931. [[CrossRef](#)]
24. Mohamad Noh, M.F.; Teh, C.H.; Daik, R.; Lim, E.L.; Yap, C.C.; Ibrahim, M.A.; Ahmad Ludin, N.; Bin Mohd Yusoff, A.R.; Jang, J.; Mat Teridi, M.A. The architecture of the electron transport layer for a perovskite solar cell. *J. Mater. Chem. C* **2018**, *6*, 682–712. [[CrossRef](#)]
25. Zhou, H.; Chen, Q.; Li, G.; Luo, S.; Song, T.b.; Duan, H.S.; Hong, Z.; You, J.; Liu, Y.; Yang, Y. Interface engineering of highly efficient perovskite solar cells. *Science* **2014**, *345*, 542–546. [[CrossRef](#)]
26. Cha, M.; Da, P.; Wang, J.; Wang, W.; Chen, Z.; Xiu, F.; Zheng, G.; Wang, Z.S. Enhancing Perovskite Solar Cell Performance by Interface Engineering Using CH<sub>3</sub>NH<sub>3</sub>PbBr<sub>0.9</sub>I<sub>2.1</sub> Quantum Dots. *J. Am. Chem. Soc.* **2016**, *138*, 8581–8587. [[CrossRef](#)] [[PubMed](#)]
27. Du, H.J.; Wang, W.C.; Ma, B.; Long, T.; Zhu, J.Z. Band Structure Adjustment of Solar Cells by Gradient Doping. *Mat. Sci. Semicon. Proc.* **2015**, *40*, 570–577. [[CrossRef](#)]
28. Li, N.; Yan, J.; Ai, Y.; Jiang, E.; Lin, L.; Shou, C.; Yan, B.; Sheng, J.; Ye, J. A low-temperature tio<sub>2</sub> /sno<sub>2</sub> electron transport layer for high-performance planar perovskite solar cells. *Sci. China Mater.* **2020**, *63*, 207–215. [[CrossRef](#)]
29. Du, H.J.; Wang, W.C.; Zhu, J.Z. Device Simulation of Lead-Free CH<sub>3</sub>NH<sub>3</sub>SnI<sub>3</sub> Perovskite Solar Cells with High Efficiency. *Chin. Phys. B* **2016**, *25*, 108802. [[CrossRef](#)]
30. Al-Mousoi, A.K.; Mohammed, M.K.; Pandey, R.; Madan, J.; Dastan, D.; Ravi, G.; Sakthivel, P. Simulation and analysis of lead-free perovskite solar cells incorporating cerium oxide as electron transporting layer. *RSC Adv.* **2022**, *12*, 32365–32373. [[CrossRef](#)]
31. Hossain, M.K.; Arnab, A.; Das, R.C.; Hossain, K.; Rubel, M.; Rahman, M.F.; Bencherif, H.; Emetere, M.; Mohammed, M.K.; Pandey, R. Combined DFT, SCAPS-1D, and wxAMPS frameworks for design optimization of efficient Cs<sub>2</sub>BiAgI<sub>6</sub>-based perovskite solar cells with different charge transport layers. *RSC Adv.* **2022**, *12*, 35002–35025. [[CrossRef](#)]
32. Gan, Y.-J.; Qiu, G.-X.; Qin, B.-Y.; Bi, X.-G.; Liu, Y.-C.; Nie, G.-C.; Ning, W.-L.; Yang, R.-Z. Numerical Analysis of Stable (FAPbI<sub>3</sub>)<sub>0.85</sub>(MAPbBr<sub>3</sub>)<sub>0.15</sub>-Based Perovskite Solar Cell with TiO<sub>2</sub>/ZnO Double Electron Layer. *Nanomaterials* **2023**, *13*, 1313. [[CrossRef](#)]
33. Lakhdar, N.; Hima, A. Electron transport material effect on performance of perovskite solar cells based on CH<sub>3</sub>NH<sub>3</sub>GeI<sub>3</sub>. *Opt. Mater.* **2020**, *99*, 109517. [[CrossRef](#)]
34. Huang, H.-C.; Yuan, E.-H.; Zhang, D.-S.; Sun, D.-X.; Yang, M.-H.; Zheng, Z.-Y.; Zhang, Z.-L.; Gao, L.; Panezai, S.; Qiu, K.-F. Free field of view infrared digital holography for mineral crystallization. *Cryst. Growth Des.* **2023**, *23*, 7992–8008. [[CrossRef](#)]
35. Klenk, R. Characterization and modeling of chalcopyrite solar cells. *Thin Solid Films* **2001**, *387*, 135–140. [[CrossRef](#)]

36. Minemoto, T.; Matsui, T.; Takakura, H.; Hamakawa, Y.; Negami, T.; Hashimoto, Y.; Uenoyama, T.; Kitagawa, M. Theoretical analysis of the effect of conduction band offset of window/CIS layers on performance of CIS solar cells using device simulation. *Sol. Energy Mater. Sol. Cell* **2001**, *67*, 83–88. [[CrossRef](#)]
37. Gloeckler, M.; Sites, J. Efficiency limitations for wide-band-gap chalcopyrite solar cells. *Thin Solid Films* **2005**, *480*, 241–245. [[CrossRef](#)]
38. Minemoto, T.; Hashimoto, Y.; Satoh, T.; Negami, T.; Takakura, H.; Hamakawa, Y. Cu(In,Ga)Se<sub>2</sub> solar cells with controlled conduction band offset of window/Cu(In,Ga)Se<sub>2</sub> layers. *J. Appl. Phys.* **2001**, *89*, 8327–8330. [[CrossRef](#)]
39. Minemoto, T.; Hashimoto, Y.; Satoh, T.; Kolahi, W.S.; Negami, T.; Takakura, H.; Hamakawa, Y. Control in conduction band offset in wide-gap Cu(In,Ga)Se<sub>2</sub> solar cells. *Sol. Energy Mater. Sol. Cell* **2003**, *75*, 121–126. [[CrossRef](#)]
40. Torndahl, T.; Platzer-Bjorkman, C.; Kessler, J.; Edoff, M. Atomic layer deposition of Zn<sub>1-x</sub>Mg<sub>x</sub>O buffer layers for Cu(In,Ga)Se<sub>2</sub> solar cells. *Prog. Appl.* **2007**, *15*, 225–235. [[CrossRef](#)]
41. Turcu, M.; Rau, U. Fermi level pinning at CdS/Cu(In,Ga)(Se,S)<sub>2</sub> interfaces: Effect of chalcopyrite alloy composition. *J. Phys. Chem. Solids* **2003**, *64*, 1591–1595. [[CrossRef](#)]
42. Tanaka, K.; Minemoto, T.; Takakura, H. Analysis of heterointerface recombination by Zn<sub>1-x</sub>Mg<sub>x</sub>O for window layer of Cu(In,Ga)Se<sub>2</sub> solar cells. *Sol. Energy* **2009**, *83*, 477–479. [[CrossRef](#)]
43. Minemoto, T.; Murata, M. Theoretical analysis on effect of band offsets in perovskite solar cells. *Sol. Energy Mater. Sol. Cells* **2015**, *133*, 8–14. [[CrossRef](#)]

**Disclaimer/Publisher’s Note:** The statements, opinions and data contained in all publications are solely those of the individual author(s) and contributor(s) and not of MDPI and/or the editor(s). MDPI and/or the editor(s) disclaim responsibility for any injury to people or property resulting from any ideas, methods, instructions or products referred to in the content.